Applied Surface Science 666 (2024) 160392

Contents lists available at ScienceDirect

Applied Surface Science

journal homepage: www.elsevier.com/locate/apsusc

Full Length Article

Early-stage silver growth during sputter deposition on SiO_2 and polystyrene – Comparison of biased DC magnetron sputtering, high-power impulse magnetron sputtering (HiPIMS) and bipolar HiPIMS

Kristian A. Reck [a], Yusuf Bulut [b,c], Zhuijun Xu [c], Suzhe Liang [c], Thomas Strunskus [a,d], Benedikt Sochor [b], Holger Gerdes [e], Ralf Bandorf [e], Peter Müller-Buschbaum [c], Stephan V. Roth [b,f], Alexander Vahl [a,d,g], Franz Faupel [a,d,*]

[a] Chair for Multicomponent Materials, Department of Materials Science, Kiel University, Kaiserstr. 2, 24143 Kiel, Germany
[b] Deutsches Elektronen-Synchrotron DESY, Notkestr. 85, 22607 Hamburg, Germany
[c] Technical University of Munich, TUM School of Natural Sciences, Department of Physics, Chair for Functional Materials, James-Franck-Str. 1, 85748 Garching, Germany
[d] Kiel Nano, Surface, and Interface Science, KiNSIS, Kiel University, Christian-Albrechts Platz 4, 24118 Kiel, Germany
[e] Fraunhofer Institute for Surface Engineering and Thin Films (IST), Riedenkamp 2, 38108 Braunschweig, Germany
[f] KTH Royal Institute of Technology, Department of Fibre and Polymer Technology, Teknikringen 56-58, 100 44 Stockholm, Sweden
[g] Leibniz Institute for Plasma Science and Technology, Felix-Hausdorff-Str. 2, 17489 Greifswald, Germany

ARTICLE INFO

Keywords:
Early growth
HiPIMS
BP-HiPIMS
Silver
GISAXS
SiO_2/PS substrate

ABSTRACT

The integration of silver thin films into optoelectronic devices has gained much interest due to their exceptional properties in terms of conductivity and compatibility with flexible substrates. For this type of application, ultra-thin layers are desirable, because of their optical transparency. Standard direct current magnetron sputtering (DCMS) is known to lead to undesirable formation of islands at low effective film thicknesses on typical substrates like SiO_2 or polystyrene (PS). Therefore, in this study, we explore high-power impulse magnetron sputtering (HiPIMS) with optional further acceleration of metal ions by biasing the substrate or an additional positive pulse (bipolar HiPIMS) for the fabrication of ultra-thin silver layers. The morphology and electrical properties of ultra-thin silver layers with selected effective thicknesses are characterized on SiO_2 and PS substrates. The growth evolution of characteristic parameters is further investigated by in-situ grazing-incidence small-angle X-ray scattering (GISAXS). The results show that HiPIMS deposition yields films with a higher density of clusters than DCMS leading to a percolation threshold at lower effective film thicknesses. This effect is amplified by further ion acceleration. Thus, we suggest HiPIMS as a promising technique for fabricating ultra-thin, conductive layers on organic and oxide substrates.

1. Introduction

Due to the insulating nature of most organic substrates, electrically conductive layers are essential components for organic electronics. Therefore, noble metals offering excellent conductivity and adequate elasticity are promising candidates for the development of high-performance conduction layers. Especially, the integration of thin silver films into organic electronic devices has gained considerable attention due to their potential combination of excellent electrical conductivity, optical transparency, and compatibility with flexible substrates. These films serve as essential components in various organic electronic applications [1], including organic light-emitting diodes (OLEDs) [2], organic photovoltaic cells (OPVs) [3–6], organic photodiodes [7], organic field-effect transistors (OFETs) [8], and sensors [9].

Sputter deposition offers meticulous control over the deposition of thin films, ensuring precision in terms of thickness, uniformity, and morphological characteristics, essential factors for optimizing device performance [10]. The versatility of sputter deposition techniques, such as direct current magnetron sputtering (DCMS) and radio frequency (RF) sputtering, allows for the deposition of films on various substrates, including flexible and temperature-sensitive materials, such as polyethylene terephthalate (PET) fabric [11] or polyimide foil [12].

* Corresponding author.
E-mail address: ff@tf.uni-kiel.de (F. Faupel).

https://doi.org/10.1016/j.apsusc.2024.160392
Received 11 March 2024; Received in revised form 17 May 2024; Accepted 25 May 2024
Available online 26 May 2024

Despite the afore-mentioned versatility, sputter deposition of ultra-thin metal layers remains challenging. Poor surface coverage and roughness necessitate extra fabrication steps, adding to the already high level of complexity and cost for vacuum systems [13,14]. Thus, it would be favorable to simplify the fabrication.

In addition to DCMS, pulsed DCMS, or RF sputtering as long established physical vapor deposition (PVD) methods, HiPIMS received a lot of interest in research and industry during the last two decades, as it can offer improved coating properties in many fields [15–20]. These effects stem from the operation of the magnetron, i.e., the plasma, with very short, intense pulses with a duty cycle below 5 % [21]. This concentration of power in short pulses results in a very dense plasma leading to a high fraction of ionized target material (typically up to 80 %) compared to DCMS typically not exceeding a few percent. These ions exhibit a higher kinetic energy (up to multiples tens of eV) that can influence film growth drastically [22,23]. For metals, HiPIMS conditions can result in films with lower roughness, higher conductivity, or larger grain sizes [24,25]. For polymer substrates, as used in this work, an increased film adhesion caused by ion etching is of great interest, as it can reduce the necessity of pre-treatment [26,27] or stabilize patterned surfaces [28].

The kinetic energy of ions can be further increased and tuned by biasing the substrate or by applying an additional positive pulse after the main negative pulse (bipolar HiPIMS) [20,29]. The main advantage of bipolar HiPIMS (BP-HiPIMS) is that it remains functional for insulating substrates. The fine control of ion energies enables tuning of several physical and morphological film properties, e.g., surface roughness, crystallinity, hardness, and density [30–32]. These potential advantages promote the use of HiPIMS despite its higher power supply requirements and commonly reported reduced deposition rate at the same average power compared to most DCMS processes [33].

Observation of early-stage growth stages necessitates a high resolution in space and time. Thus, grazing-incidence small-angle X-ray scattering (GISAXS) as a non-invasive and versatile scattering method, capable of exploring the interface between the substrate and the developing deposited thin metal film in situ, is chosen [34]. The main advantages of GISAXS, in comparison to direct imaging methods such as atomic force microscopy (AFM) or scanning electron microscopy (SEM), include greater statistical relevance due to a significantly larger scanned area and a larger probing depth, enabling a study of structures in the subsurface region [35].

The development of nanostructure during film formation of noble metals on polymers has been studied extensively via DCMS in the past and provides a solid foundation for comparison, data evaluation and interpretation [36–38]. Especially the reported effect of the deposition rate during nucleation has to be considered when comparing different deposition conditions [39].

Despite the broad interest in application of ultra-thin percolated Ag thin films, the role of the early stages of silver film growth for the resulting film properties has not been studied with respect to the effects of HiPIMS and a further increased ion energy by a substrate bias or BP-HiPIMS.

In this study we compare DCMS and HiPIMS deposition of Ag on technologically relevant substrates, namely SiO_2 and PS. The aim of this study is to explore the impact of ion acceleration on the early stage growth of Ag. An optional fixed DC substrate bias is utilized for DCMS and HiPIMS alike. Additionally, BP-HiPIMS is applied to compare the different approaches of ion acceleration. As substrates, pre-cleaned Si wafers with a native oxide layer are used as a well-defined reference, and spin-coated polystyrene films are used as the polymeric surface, e.g., used for organic field-effect transistors (OFETs) [40]. The morphology of ex-situ samples at different film thicknesses is analyzed by scanning electron microscopy (SEM) and the films resistances are tested. For DCMS and HiPIMS with a grounded substrate, in-situ GISAXS measurements are conducted to gain a profound understanding of film formation from early stages until a closed film is formed.

2. Materials and methods

Silicon wafers (N-type, ⟨100⟩, Siegert Wafer), diced into 12 × 15 mm^2 pieces are cleaned in an ultrasonic bath, first in acetone and consecutively in isopropanol for 10 min each. The cleaned silicon wafers possess a native oxide layer and are used directly as substrates. Polystyrene (320,000 g/mol, Carl Roth GmbH + Co. KG) is dissolved in toluene (99.8 %, Carl Roth GmbH + Co. KG) with a concentration of 21.6 mg/ml. For a complete dissolution, the solution undergoes heat treatment at 45 °C and is stirred for 1 h. The cleaned silicon pieces are coated with PS in a spin coater (WS-650MZ-23NPPB, Laurell Technologies Corporation). Using static dispense spin coating, 250 µL solution are applied and with a delay of maximum 10 s the piece is rotated at 6 krpm for 60 s with an acceleration of 3 krpm/s. The resulting thickness of PS thin films is measured with a profilometer (DektakXT, Bruker Corporation) to be $d = (40 \pm 10)$ nm preventing any influence of the underlying Si substrate on the growth of the silver layers [41].

A custom-built sputter deposition chamber for synchrotron experiments is used [28]. The unbalanced magnetron with Ag-target (diameter 2″ (50.8 mm), thickness 0.125″ (3.175 mm), 99.99 % purity) can be operated with DCMS, HiPIMS or BP-HiPIMS. For DCMS an MDX 500 (Advanced Energy), for HiPIMS a HiPSTER 1 (Ionautics AB) charged by a SR-1-N-1200 (Technix) and for BP-HiPIMS an IMPULSE 2–2 (Starfire Industries) charged by a M600DC-PS (Prevac) were used. The chamber is evacuated to a pressure of 10^{-6} mbar before a flow of 10 sccm Ar (99.999 % purity) is introduced by a mass flow controller (AX-MC-200SCCM-D, Apex Vacuum LLC) to reach a pressure of 0.35 Pa. The deposition rate is monitored by a quartz crystal microbalance STM-100 (Sycon Instruments). For DCMS, the discharge voltage is displayed by the power supply, in case of (BP-)HiPIMS, the voltage and current waveforms of pulses are monitored by an oscilloscope DSO1002A (Agilent Technologies) connected to the monitoring ports of HiPSTER 1 or IMPULSE 2–2. When the discharge has reached a steady state, the synchrotron measurement starts and the deposition begins by opening a pneumatic shutter controlled by the beamline. Precise measurements for the deposition rate for each sample are performed via GISAXS evaluation.

For fabrication of ex-situ samples with a defined film thickness, the deposition rate is determined beforehand by a profilometer (DektakXT, Bruker) for an Ag film thickness of at least 250 nm. The deposition rate is assumed to be constant over time, i.e., the film thickness is assumed to increase linearly, independent of growth state. Table 1 shows an overview of experimental parameters for ex-situ deposition. The parameters for in-situ samples are shown in Table 2. The slight differences between in-situ and ex-situ parameters is due to the optimization of ex-situ parameters to enhance the effect of ion energies based on findings from the in-situ studies. Figures S1-S4 show the temporal evolution of voltage and current of HiPIMS with the parameters used in this study. An automated

Table 1
Experimental parameters for ex-situ deposition conditions. For BP-HiPIMS, respective values for the negative and positive pulse are displayed.

Parameters	DCMS -ground	DCMS -bias	HiPIMS -ground	HiPIMS -bias	BP -HiPIMS
Voltage (V)	−310		−960		−991/ +60
Pulse Length (µs)	–		20		20/200
Delay (µs)	–		–		5
Frequency (Hz)	–			150	
Avg. Power (W)	21		32		37
Peak Current Density (A/ cm^2)	0.003			0.80	
Degree of Ionization (%)	3.5			58.2	
Pressure (Pa)			0.35		
Ar Flow /(sccm)			10		
Substrate Bias (V)	Gnd	−60	Gnd	−60	Gnd
Deposition Rate (Å/s)	2.8	2.7	2.0	1.6	1.8

Table 2
Experimental parameters for in-situ deposition conditions.

Parameters	DCMS -SiO_2	DCMS -PS	HiPIMS -SiO_2	HiPIMS -PS
Voltage (V)	−313	−310	−672	−976
Pulse Length (μs)	–		20	
Frequency (Hz)	–		810	150
Avg. Power (W)	27	23	35	40
Peak Current Density (A/cm^2)	0.004	0.004	0.26	1.14
Pressure (Pa)		0.35		
Ar Flow (sccm)		10		
Substrate Bias (V)		Gnd		
Deposition Rate (Å/s)	3.3	2.7	2.7	2.6

pneumatic shutter system allows a deposition time control with ± 0.1 s precision for achieving the respective desired film thickness.

For detection of sputtered ions and neutrals, a Quantum System (Impedans Ltd.) consisting of a combination of a retarding field energy analyzer (RFEA) and a quartz crystal microbalance (QCM) as collection electrode is used [42]. Hence, this system can measure the ion energy density function (IEDF) and degree of ionization at the position of the substrate. The IEDF is measured by monitoring the current at the collection electrode while ramping the repelling voltage for blocking ions depending on their kinetic energy. For determining the degree of ionization of the target material, the frequency of the QCM is monitored while the repelling voltage is switched 10 times between two states: either blocking no ions (0 V) or blocking all ions (+200 V). The duration of each state is set to 10 s. Thus, the change of frequency is either related to neutrals and ions or just neutrals. The sensor itself is grounded.

Field emission scanning electron microscopy images were taken with a Zeiss Gemini Ultra55 Plus (Carl Zeiss) at a low acceleration voltage of 2 kV and a low working distance of ≈ 2 mm with the in-lens detector. For visualization and normalization of brightness and contrast the software GIMP (GIMP Development Team, version 2.10.32) is used. The software ImageJ (Wayne Rasband, version 1.54d) was used to systematically analyze the surface coverage. One exemplary image processing necessary for determining surface coverage is shown in Figure S5. Typical structure size is determined by intersect method for seven lines per image.

The in-situ grazing-incidence small-angle X-ray scattering (GISAXS) experiments were conducted at the microfocus small- and wide-angle X-ray scattering (MiNaXS) beamline P03 at the synchrotron PETRA III at DESY [43]. The X-ray with a wavelength of $\lambda = 0.105$ nm and a size of around 30 × 25 μm^2 hits the sample at an incident angle of 0.4°. At a distance of 3.415 m behind the samples, a Dectris Pilatus 2 M detector with a pixel size of 172 × 172 μm^2 is used to record at framerate of 20 frames per second during sputter deposition. To minimize scattering at air after the sample, an evacuated flight tube is placed in front of the detector. The DPDAK software package (version 1.5) is used for the data processing of 2D GISAXS detector patterns [44]. Figure S6 shows the sputter deposition chamber mounted at beamline P03.

The resistance of the silver thin films is measured with a custom-built probe card with spring contacts attached to Signatone H-150 probe station with plateau lift. The spring contacts at a distance of 9 mm to each other ensure optimal contact and as less damage to the surface as possible. The contacts are connected to an HP 34401A (Hewlett-Packard) operated in 2-wire mode. The resistance at three positions on each sample is recorded.

3. Results and discussion

Silver is deposited on SiO_2 and PS for different PVD conditions in order to investigate the influence of ionization and kinetic energy of silver atoms on the morphology, growth kinetics and electrical resistance.

Therefore, the ion energy density functions and degrees of ionization for the different PVD methods used in our study are determined beforehand. Afterwards, ex-situ samples for certain film thicknesses are characterized by SEM and electrical measurements for DCMS and HiPIMS with either grounded or biased substrate and for BP-HiPIMS. At last, for selected parameters (DCMS-ground and HiPIMS-ground) in-situ GISAXS studies are discussed in detail.

3.1. Ion energy density functions and degrees of ionization

For characterisation of the deposition conditions, a plasma sensor consisting of an RFEA and QCM is used. This sensor is chosen, as it can measure the two most important distinguishing parameters between DCMS and any HiPIMS process at the location of the substrate: the IEDF and degree of ionization of target material.

Fig. 1 shows the IEDFs of Ag for DCMS-ground, HiPIMS-ground, and BP-HiPIMS. The Ag ions found in the DCMS plasma show a peak for a kinetic energy of 1 eV which is quickly decreasing for higher energies. For energies higher than 5 eV no ions are detected. For the HiPIMS-ground plasma, the Ag ions show a similar peak at 1 eV with a quick reduction up to 5 eV as well. However, this thermalized peak is followed by a more energetic tail of ions up to 35 eV. To the best of our knowledge, no IEDFs of Ag for HiPIMS have been published so far, however these results agree qualitatively with observations for other target materials. A thermalized peak near 0 eV and high energetic tail up to 40 eV for Ti^+ ions [45] or up 60 eV for Cr^+ ions [22] is found.

For BP-HiPIMS, the positive pulse of +60 V following the negative HiPIMS pulse shows a tremendous effect on the IEDF. Only a small peak of thermal ions is detected. Most of the Ag ions possess a higher kinetic energy of up to 65 eV with a peak at 56 eV due to the acceleration in the electric field during the positive pulse. Other studies applying energy-resolved mass spectroscopy for BP-HiPIMS ions showed an almost exact shift of the narrow thermal peak by the positive pulse voltage and fast ions showing kinetic energies exceeding the positive pulse voltage [20,29,46,47]. The IEDF in this work shows a different course. However, another study that used a RFEA as well [48], reported IEDFs where the kinetic energy of most ions did not reach the energy corresponding the positive pulse voltage by a few eV.

Besides their energy, the ratio of ions to neutral atoms is also crucial for understanding the effect of the PVD process. Independent of the deposition rate, the degree of ionization P_i is defined by

$$P_i = \frac{J_i}{J_n + J_i}$$

with the flux of ions J_i and flux of neutral atoms J_n.

This ratio is measured for DCMS and several HiPIMS conditions (see Table S1, some are not used otherwise in this publication) and are displayed in Fig. 2. Due to findings in [49,50], which suggest a strong dependence of P_i on the peak current density or pulse power density respectively, P_i is plotted as a function of the corresponding peak current density. As expected, DCMS shows a quite low P_i of maximum 3.2 % for a peak current density of 0.003 A/cm^2 which agrees with reported degrees of ionization for DCMS [49,51]. The highest P_i of (65 ± 5) % is present for the highest peak current density of (1.28 ± 0.04) A/cm^2 for HiPIMS. The conditions for deposition of ex-situ and in-situ samples are marked in Fig. 2 with respective windows for DCMS, HiPIMS with a frequency of 810 Hz (in-situ deposition on SiO_2) and HiPIMS with a frequency of 150 Hz (ex-situ deposition and in-situ deposition on PS, denoted HiPIMS-810 and HiPIMS-150 respectively).

These results show in fact, that HiPIMS provides energetic ions compared to DCMS and can lead to a high degree of ionization for silver as target material as well.

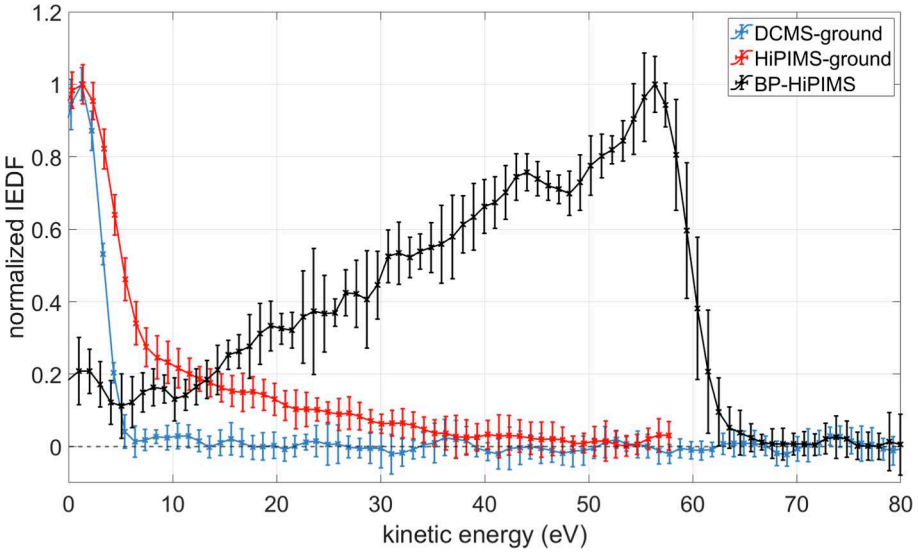

Fig. 1. Normalized ion energy density function (IEDF) of Ag ions for DCMS-ground, HiPIMS-ground and BP-HiPIMS. Error bars correspond to ±1σ.

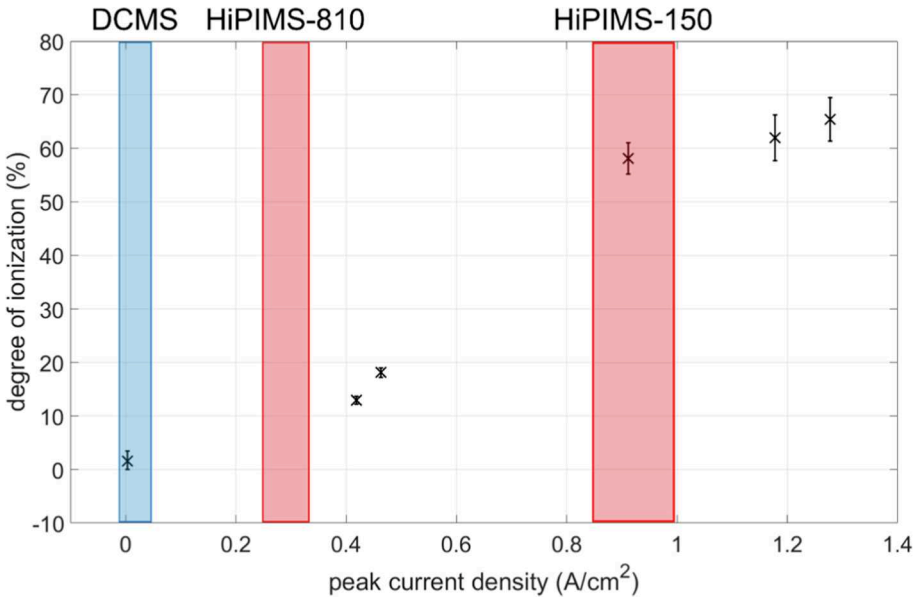

Fig. 2. Degree of ionization of Ag atoms for DCMS and different HiPIMS parameter reaching the substrate. Ranges of operation for DCMS and HiPIMS with different frequencies for deposition of ex-situ and in-situ samples are marked by blue and red boxes, respectively. Error bars correspond to ±1σ. (For interpretation of the references to colour in this figure legend, the reader is referred to the web version of this article.)

3.2. Morphological and electrical characterization of the deposited Ag thin films

For analyzing different stages during film growth, ex-situ samples are prepared for the conditions DCMS-ground, DCMS-bias, HiPIMS-ground, HiPIMS-bias and BP-HiPIMS on both SiO_2 and PS with effective Ag film thicknesses δ_{Ag} of 2, 3, 4, 6, 10, 20 and 300 nm, respectively.

In Fig. 3 an overview of SEM images for the afore-mentioned PVD methods and different film thicknesses are shown for SiO_2 as substrate. Fig. 4 a) displays the ratio of surface area covered by Ag and Fig. 4 b) indicates the results of electrical characterization. As percolation occurs well below $\delta_{Ag} = 10$ nm, these ex-situ electrical measurements possess an unknown uncertainty near the percolation threshold and do not allow an exact determination. However, as a general trend, DCMS shows equal or later percolation threshold compared to HiPIMS. Thus, the focus of interpretation is of the overall trends and comparisons rather than singular values. All PVD methods lead to the formation of Ag islands or clusters for layers with an effective thickness of $\delta_{Ag} = 2$ and 3 nm, see Fig. 3. This behavior is well known and reported in literature [37]. The SEM images in Fig. 3 also show some larger clusters for $\delta_{Ag} \leq 4$ nm as brighter spots, originating from the coalescence of two or more smaller clusters.

For $\delta_{Ag} = 4$ nm, an additional sequence of SEM images with higher magnification is provided in Figure S7. The islands for DCMS-bias and HiPIMS-ground show mostly a circular shape due to the attachment of additional sputtered Ag and coalescence of small islands. However, the morphology of DCMS-ground, HiPIMS-bias and BP-HiPIMS differs. Here, the SEM images show larger irregular shaped clusters or domains with higher aspect ratios as well. This effect can be related to the kinetic energy of arriving Ag ions of HiPIMS-bias and BP-HiPIMS being elevated by the negative bias or positive pulse, respectively. These fast ions could lead to the creation of surface defects or could be implanted, reducing

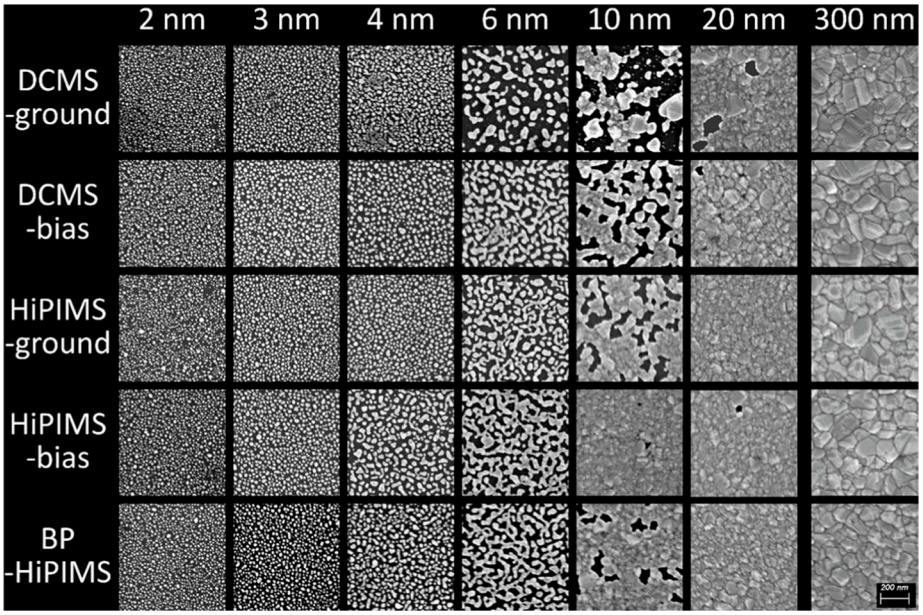

Fig. 3. SEM images of sputtered Ag on SiO_2 for five different sputter conditions taken at different film thicknesses. The scalebar applies to all SEM images.

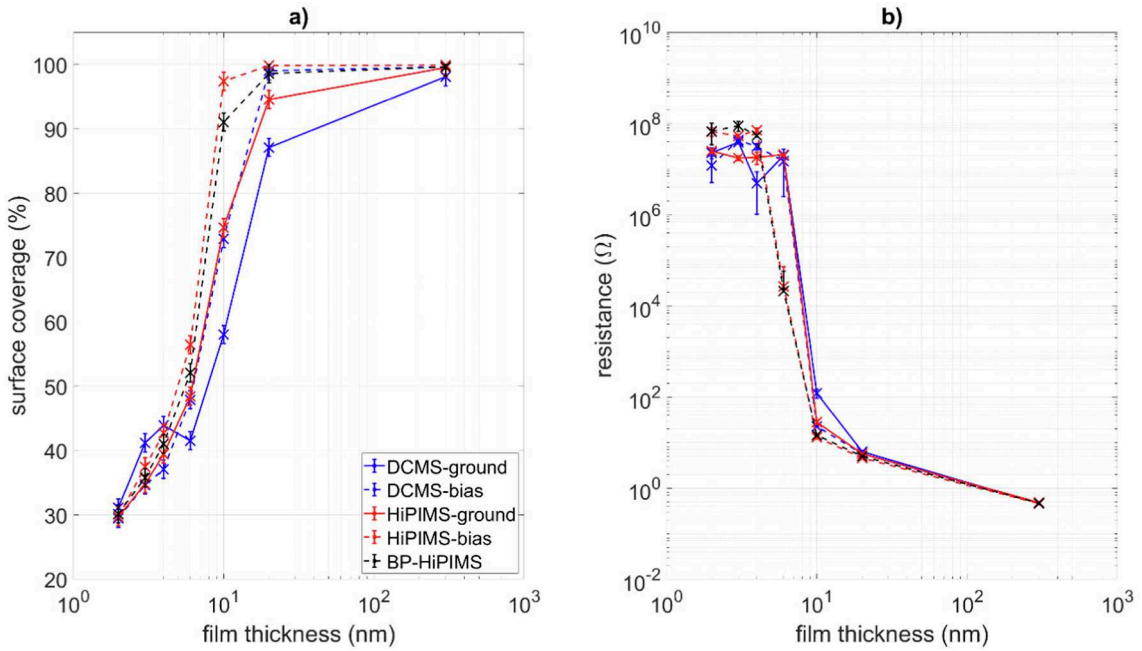

Fig. 4. A) Surface coverage (SEM) and b) electrical resistance over 9 mm distance as function of the effective Ag film thickness for SiO_2 as substrate. Error bars correspond to ±1σ.

surface diffusion, hence providing additional nucleation sites that prevent the reduction of surface energy by forming more round shapes [52]. The reasons for the same behavior of DCMS-ground are unclear.

Up to δ_{Ag} = 4 nm, all samples show insulating behavior with resistances above 1 MΩ, which is expected for non-closed, non-percolated thin films. This result also shows that the native SiO_2 layer on top of the Si wafer is completely insulating and does not influence this measurement.

At δ_{Ag} = 6 nm enough silver is present to form elongated domains for all deposition conditions. For HiPIMS-bias and BP-HiPIMS, the domains possess many connections between each other, due to the aforementioned reasons. HiPIMS-ground and DCMS-bias exhibit some connected domains, while for DCMS-ground most domains are separate. These morphological differences are also reflected in the electrical properties. The Ag thin films deposited by HiPIMS-bias and BP-HiPIMS show an almost identical reduction in resistance, indicating the existence of a path for electrical conduction while the thin films deposited by the other techniques remain completely insulating. This result indicates that the connections for HiPIMS-ground and DCMS-bias are not far reaching.

The effective film thickness of δ_{Ag} = 10 nm reveals the largest influence of PVD method. While both DCMS processes produce branched domains, HiPIMS-bias and BP-HiPIMS already form an almost closed film, with a surface coverage above 90 %, see Fig. 4 a). HiPIMS-ground still leads to connected domains but offers a slightly higher surface coverage than DCMS-bias and a much higher surface coverage than

DCMS-ground. For $\delta_{Ag} = 10$ nm, all samples are above the percolation threshold showing a greatly reduced resistance. However, the samples fabricated by HiPIMS-bias and BP-HiPIMS show the lowest resistance in comparison. This trend continues for $\delta_{Ag} = 20$ nm and $\delta_{Ag} = 300$ nm. At $\delta_{Ag} = 20$ nm all silver layers are closed whereas the DCMS-ground layer is still slightly porous. For $\delta_{Ag} = 300$ nm the SEM images show closed layers consisting of larger structures than at $\delta_{Ag} = 20$ nm. For instance, DCMS-ground exhibits an average structure size of (75 ± 13) nm while BP-HiPIMS exhibits (63 ± 15) nm. Due to the high thickness, no direct influence of the early growth stage on the film structure is expected.

To summarize, the evolution of morphology is mainly influenced by the increased kinetic energy of HiPIMS-bias and BP-HiPIMS by creating more nucleation sites resulting in an earlier percolation threshold, a higher surface coverage, and lower resistance for every effective film thickness. Biasing the substrate for DCMS shows a slightly higher surface coverage, but the effect is marginal compared to HiPIMS-bias and BP-HiPIMS. The reduced effectivity is related to low number of ions present in DCMS. For HiPIMS-ground it seems the high number of ions with a slight elevation of kinetic energy compared to DCMS is not sufficient for strongly influencing the morphology. The similarity of HiPIMS-bias and BP-HiPIMS indicate that both techniques influence film growth in almost the same way, see Fig. 4.

Fig. 5 shows the SEM images of Ag thin films on PS for the same parameters as for SiO_2 in Fig. 3. In Fig. 6 a), the corresponding surface coverage and in Fig. 6 b) the electrical resistance are shown. The overall evolution of thin film morphology is similar to SiO_2; thus, the focus of discussion is on differences to SiO_2. At $\delta_{Ag} = 4$ nm the PS ex-situ samples already start to show larger coalesced clusters and domains, at a lower effective film thickness compared to SiO_2. Both DCMS processes primarily show coalesced clusters while all HiPIMS process produce primarily larger domains resulting in a higher surface coverage, shown in Fig. 6 a). The domains of HiPIMS-bias and BP-HiPIMS show more branches than HiPIMS-ground. Directly noticeable is the earlier percolation of most of the thin films at $\delta_{Ag} = 4$ nm, between 2 nm and 6 nm earlier than for SiO_2.

On the one hand, for $\delta_{Ag} = 6$ nm and $\delta_{Ag} = 10$ nm, the DCMS processes lead to branched domains similar to SiO_2 for the same effective film thicknesses. On the other hand, all HiPIMS techniques result in almost or completely closed thin films already at $\delta_{Ag} = 6$ nm. Again, HiPIMS-bias and BP-HiPIMS provide the highest surface coverage, but the discrepancy to HiPIMS-ground is less pronounced than for SiO_2. At $\delta_{Ag} = 20$ nm all samples show a closed film with some minor defects, which are not present for $\delta_{Ag} = 300$ nm. The mean size of Ag structures is slightly reduced by HiPIMS processes. For example, DCMS-ground exhibits a structure size of (76 ± 8) nm while BP-HiPIMS leads to (61 ± 9) nm. So, for both substrates, BP-HiPIMS leads to smaller structure sizes than DCMS-ground. This effect is commonly reported as one potential mechanism for a higher hardness of HiPIMS coatings [53,54]. However, this observation contradicts the observation of larger grain sizes of Ag for HiPIMS in [24]. To investigate this contradiction more closely, AFM measurements are conducted on all Ag films with $\delta_{Ag} = 300$ nm deposited by DCMS-ground and BP-HiPIMS. The experimentally obtained RMS roughness is listed in Table S2. The films prepared by BP-HiPIMS show a slightly lower roughness than for DCMS-ground, which agrees with the results in [24]. Potential explanation for the lower resistance and smaller structure size present for BP-HiPIMS in this study is the analysis by SEM, which can only indicate boundaries between grains and other structures on the surface of the film.

Overall, HiPIMS-bias and BP-HiPIMS provide the lowest resistance at every effective film thickness while both DCMS processes exhibit the highest resistance for $\delta_{Ag} \geq 6$ nm. The thin films prepared by HiPIMS-ground interestingly are not percolated at $\delta_{Ag} = 4$ nm while both DCMS films are percolated. However, at $\delta_{Ag} = 6$ nm HiPIMS-ground shows percolation and significant lower resistance than DCMS. One possible explanation with regards to the morphology in Fig. 5 are two different percolation mechanism at $\delta_{Ag} = 4$ nm. On the one hand, DCMS samples primarily show coalesced clusters, which can be formed due to higher surface diffusion of small cluster and atoms. These clusters are connected by thin ridges. Preferably, impinging atoms tend to adhere on the surface of a cluster which is close to the surface of another cluster. These structures have a high out of plane aspect ratio, resulting in a lower surface coverage, see Fig. 6 a). Their higher lateral aspect ratio is known to reduce the percolation threshold. Thus, conductivity is mediated by a limited number of spatial separated electrical paths. On the other hand, HiPIMS-bias and BP-HiPIMS mainly lead to domains, because high energetic ions create more nucleation centers limiting surface diffusion. These structures exhibit a lower aspect ratio, thus show a higher surface coverage. Conductivity is then mainly achieved when the domains touch each other. Conduction is related to a high density of electrical paths, i.e., lower resistance. The ions of HiPIMS-ground offer an intermediate kinetic energy leading to an intermediate growth state at $\delta_{Ag} = 4$ nm. The resulting aspect ratio is neither low

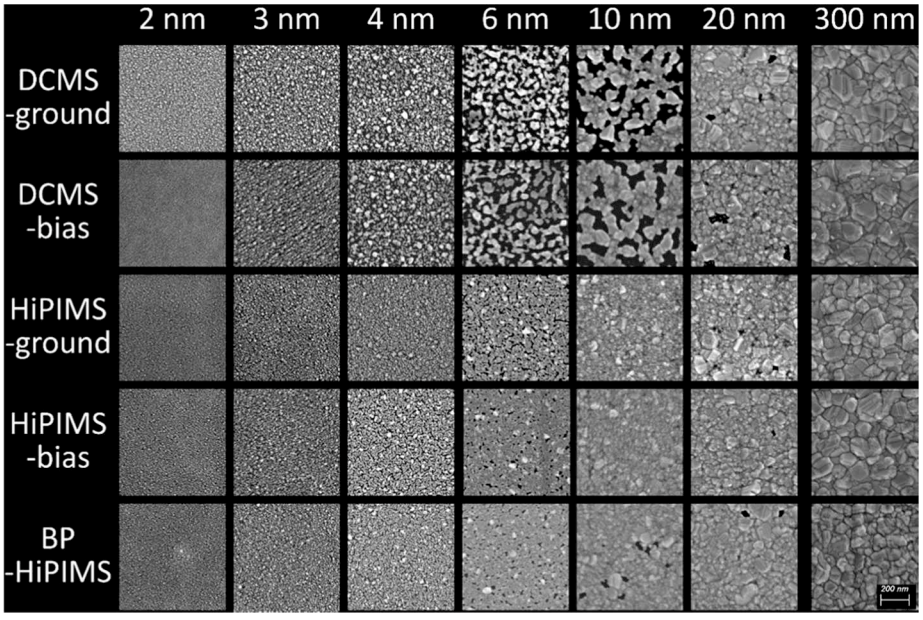

Fig. 5. SEM images of sputtered Ag on PS for five different sputter conditions taken at different film thicknesses. The scalebar applies to all SEM images.

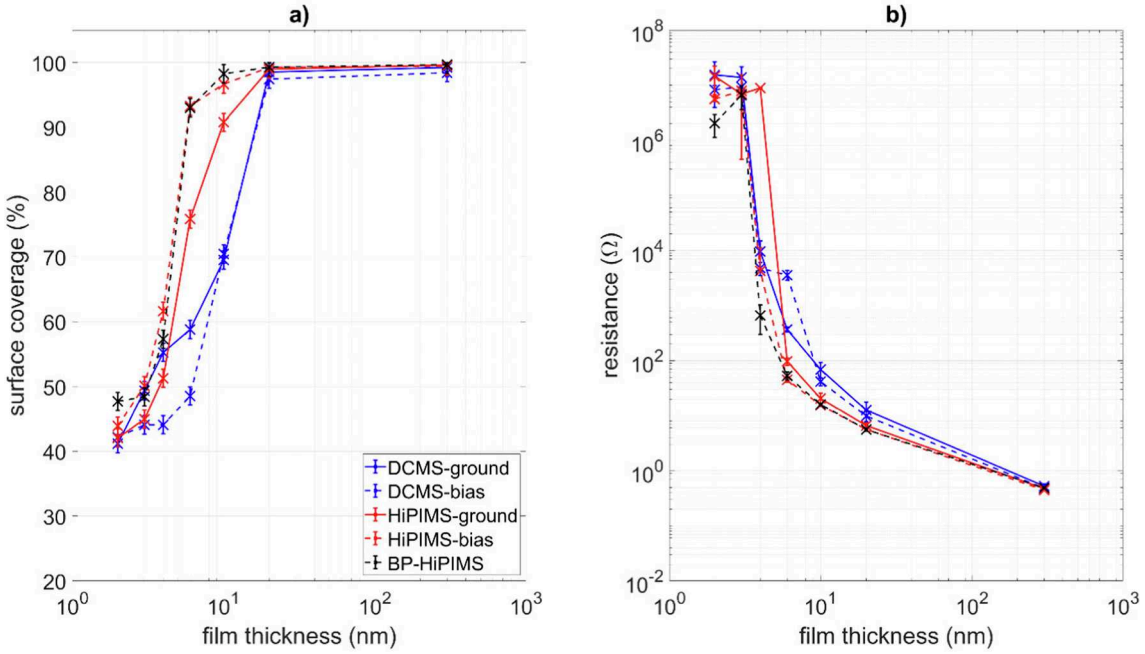

Fig. 6. A) Surface coverage (SEM) and b) electrical resistance over 9 mm distance as function of the effective Ag film thickness for PS as substrate. Error bars correspond to ±1σ.

enough to establish conductivity via touching adjacent domains nor high enough to achieve conduction via thin ridges. Once conduction is achieved at $\delta_{Ag} = 6$ nm by touching adjacent domains, the resistance is closer to HiPIMS-bias and BP-HiPIMS than to DCMS.

The intermediate kinetic energy of ions from HiPIMS-ground appears to be sufficiently high to generate nucleation sites in the polymer. This has a beneficial effect in forming a closed layer at lower effective film thicknesses compared to DCMS. This is the main difference compared to Ag growth on SiO_2.

3.3. Morphological Ag thin film evolution during sputter deposition using in situ GISAXS

To further explore the differences between DCMS and HiPIMS, the afore-mentioned survey of various ex-situ samples is extended by selected in-situ deposition experiments using GISAXS to obtain a continuous morphological characterization. The GISAXS technique allows for monitoring the evolution of the Ag thin film nanostructure with a high temporal resolution and good statistics. For these studies, two PVD methods are selected: DCMS-ground and HiPIMS-ground are chosen because they are the most common and widely used PVD processes and are not affected by an individually selected bias or positive pulse voltage, which are dependent on the specific application. The exact parameters differ slightly from afore-mentioned ex-situ parameters and are displayed in Table 2. Each in-situ study starts with an uncoated substrate, SiO_2 or PS, for a fixed duration of Ag sputter deposition.

For the correlation of each detector frame with the corresponding effective film thickness, a precise determination of the deposition rate is necessary. To do so, the intensity distribution along the q_z axis at the last frame (highest thickness) of each sample is fitted with multiple Lorentzian functions, according the number of present maxima. The final film thickness is given by

$$\delta_{final} = \frac{n2\pi}{|\Delta q_z|},$$

with Δq_z the difference in wavenumbers of the Lorentzian fit positions with the lowest and highest wavenumber of the thickness maxima and n the number of orders. This procedure is exemplarily shown in Figure S8.

For a known deposition time t_d, a constant deposition rate of

$$R_d = \frac{\delta_{final}}{t_d}$$

is assumed and used to determine the effective film thickness at every frame.

Fig. 7 shows the in-situ evolution of the mean Ag cluster distance for deposition on a SiO_2 substrate and Fig. 8 the corresponding deposition on PS with DCMS-ground and HiPIMS-ground. The mean cluster distance (D) is related to the position of the intensity peak along the q_y-axis. Generally, this peak appears as soon as sufficient material is deposited to form a locally correlated Ag nanostructure. During further deposition, the peak position is shifted from larger q_y (smaller cluster distance) to smaller q_y (larger cluster distance) values. The peak position is determined by fitting a Lorentzian function to the horizontal line cut of every detector frame i. Figure S9 show a sequence of exemplary detector images and their respective evaluation. The distance between neighboring clusters is of course distributed, thus the peak position is associated with the mean cluster distance, which is calculated by

$$D_i = 2\pi/q_{y,i}.$$

For effective film thicknesses of $\delta_{Ag} \leq 0.5$ nm the detection of this structure peak is not possible, because the amount of Ag on the surface is not high enough to provide a detectable scattering length density. When a locally correlated Ag nanostructure is formed by diffusion-mediated coalescence of atoms, the mean cluster distance D can be observed. This coalescence continues up to $\delta_{Ag} \approx 4$ nm shown by an almost linear increase in D for DCMS-ground and HiPIMS-ground. Both PVD methods show almost identical mean cluster distances, indicating that this growth stage is not influenced by the PVD method. This result agrees with SEM images in Fig. 3, which show no significant differences between DCMS-ground and HiPIMS-ground at $\delta_{Ag} = 2$ nm and $\delta_{Ag} = 3$ nm. For $\delta_{Ag} \geq 4$ nm, the slope for HiPIMS-ground is reduced considerably resulting in a much lower D compared to DCMS-ground, while the slope of DCMS-ground remains almost unchanged until $\delta_{Ag} = 7$ nm. In other terms, HiPIMS-ground results in a much higher density of clusters for $\delta_{Ag} \geq 4$ nm than DCMS-ground. This finding is related to a reduced mean

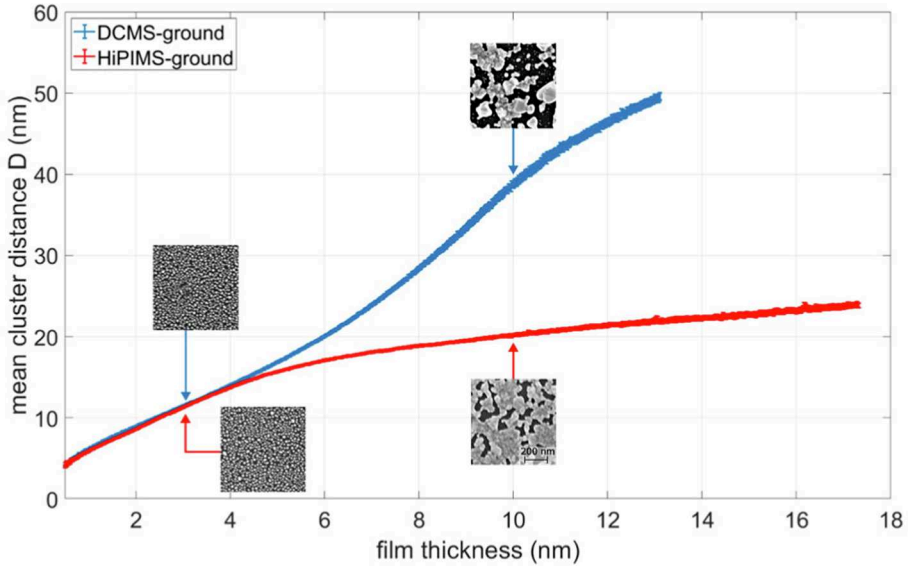

Fig. 7. In-situ evolution of the mean Ag cluster distance forming on SiO_2 with ex-situ SEM insets at corresponding effective film thicknesses. Error bars correspond to ±3σ. The scalebar applies to all SEM images.

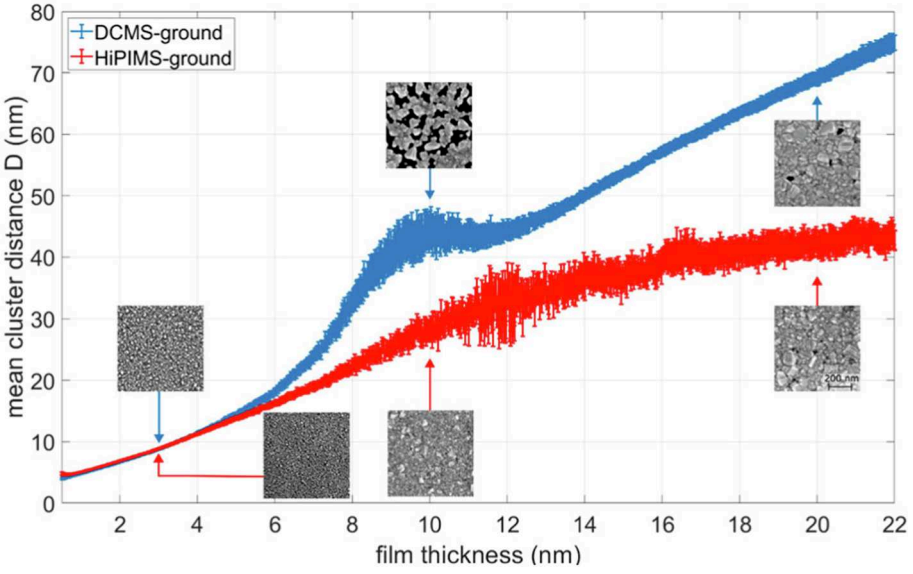

Fig. 8. In-situ evolution of the mean Ag cluster distance forming on PS with ex-situ SEM insets at corresponding effective film thicknesses. Error bars correspond to ±3σ. The scalebar applies to all SEM images.

diffusion length during HiPIMS, because of the creation of surface defects acting as nucleation points. Nevertheless, it seems this effect is not present for effective film thicknesses $\delta_{Ag} \leq 4$ nm. One possible explanation is that a reduced mean diffusion length is not directly related to the effective film thickness, but rather with the duration of the process. Each substrate possesses a certain number of surface defects prior to the deposition. The number of these vacant defects is reduced over time by occupation of nucleating Ag atoms. However, new defects can be created by high-energetic ions or photons from the plasma. The flux of energetic particles is constant over time; thus, the rate of defect creation on an uncovered substrate surface is constant as well. Assuming a lifetime of these defects of at least multiple seconds [55], the creation of defects is in competition with depletion by nucleation. Therefore, the delayed effect and reduction of the slope for $\delta_{Ag} \geq 4$ nm of HiPIMS can be related to the increased creation of defects compared to DCMS, which exhibits a depletion of defects for $\delta_{Ag} \geq 4$ nm.

The difference between D of DCMS-ground and HiPIMS-ground increases until the end of the in-situ sequences. In comparison with the morphology in Fig. 3 at $\delta_{Ag} = 10$ nm, the GISAXS measurement reflects the morphology differences well. On the one hand, the presence of large, barely connected domains for DCMS-ground result in low number of scattering centres, thus exhibiting a higher mean cluster distance. On the other hand, small, heavily branched domains for HiPIMS-ground result in a higher density of scattering centers, corresponding to lower D values.

In Fig. 8 the mean cluster distances of Ag on PS with DCMS-ground and HiPIMS-ground up to $\delta_{Ag,\ final} = 22$ nm are shown. Reasons for different $\delta_{Ag,\ final}$ values between samples are slight differences in deposition rate and choice of deposition time. In Figure S10 the mean cluster distances of both substrates, SiO_2 and PS, are shown.

On PS, both processes result in an almost identical distance of clusters up to $\delta_{Ag} = 4$ nm as well. Compared to SiO_2, the distance at $\delta_{Ag} = 4$

nm of (11.3 ± 0.3) nm is lower than (13.8 ± 0.3) nm of SiO_2. Therefore, regardless of the PVD method, the surface of PS limits the mean diffusion length of Ag atoms and leads to smaller clusters with a higher density compared to SiO_2. For $\delta_{Ag} \geq 4$ nm, in contrast to Ag deposition on SiO_2, the slope of HiPIMS-ground shows only a slight reduction while the slope of DCMS-ground increases drastically up to $\delta_{Ag} = 9$ nm where the distance remains almost constant up to $\delta_{Ag} = 12$ nm. After this plateau, the distances increase again at constant rate. These two different evolutions can be explained by the morphology evolution of the SEM images in Fig. 5. The greatly increased slope of DCMS-ground for 4 nm $\leq \delta_{Ag} \leq$ 9 nm is related to the formation of a large branched domain structure due to coalescence, reducing the number of scattering centers, i.e., increasing the mean distance between clusters. Once the branched domains reached their nearest neighbors, the growth is dominated by adsorption of incoming Ag atoms on already existing domains rather than creating new nuclei. During this stage, the distance between domains remains constant – forming the plateau. The distance starts to increase again when holes between domains start to close and domains grow together. On the other hand, the HiPIMS-ground thin film shows a much higher surface coverage, with the film at $\delta_{Ag} = 10$ nm being completely closed. Hence, the thin film evolution is dominated by domain coarsening for 4 nm $\leq \delta_{Ag} \leq 10$ nm and reduction of structure boundaries for $\delta_{Ag} \geq 10$ nm. Thus, the larger structures found at $\delta_{Ag} =$ 20 nm for DCMS-ground mainly originate from a coarser morphology present during film formation. The finer morphology of HiPIMS-ground during growth and having a higher surface coverage leads to smaller structures throughout the whole deposition process.

As a final step, the presented results facilitate a comparison and extension of the morphological regimes reported by Schwartzkopf et al. [37] during the film growth of gold deposited on PS by DCMS. For this purpose, the morphologies of DCMS-ground and BP-HiPIMS during growth on PS are displayed in Fig. 9. BP-HiPIMS is selected as its features deviate most from DCMS-ground. During the first two phases of nucleation and partial coalescence, BP-HiPIMS shows no significant influence, resulting in a similar morphology. In this work, it was not possible to distinguish between phase I and phase II, namely nucleation or partial coalescence. During phase III, the morphology of DCMS-ground is characterized by the coalescence of clusters into large domains where conductivity is formed by connected domains. Those conductive paths are marked in blue in Fig. 9. BP-HiPIMS, on the other hand, leads predominantly to the growth of already existing clusters, resulting in a conductive, almost closed layer. After further deposition of Ag, the differences reduce and during phase IV, the layer growth, the morphologies become similar again.

4. Conclusion

The results of this study show that the choice of PVD methods, namely DCMS or HiPIMS, has a crucial influence on film morphology and electrical performance of ultra-thin Ag layers deposited on oxide and organic substrates. The greatly enhanced ratio of ionized to neutral target atoms and their increased kinetic energy by using HiPIMS has the potential to create more surface defects that act as nucleation centers resulting in a higher surface coverage before a completely closed film is formed. This effect is pronounced for the polymer substrate PS but very limited for the SiO_2 substrate. The higher bonding energies of SiO_2 hinder the creation of defects. These higher bonding energies can, however, be surmounted by further ion acceleration with a substrate bias or BP-HiPIMS, changing the surface morphology significantly compared to DCMS. Overall, HiPIMS with additional substrate bias and BP-HiPIMS produced thin films with the highest surface coverage and the least electrical resistance during the whole film growth and earliest percolation threshold. Thus, HiPIMS shows many beneficial effects for fabricating ultra-thin silver layers for optoelectronic devices, e.g., organic photovoltaics, indicating the potential to be further optimized by precise control of ion energies.

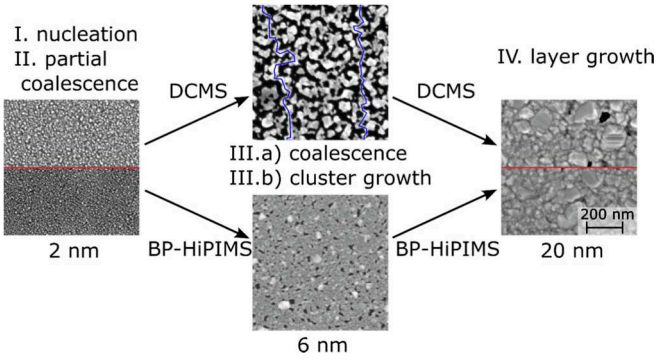

Fig. 9. Schematic course of Ag film growth deposited by DCMS-ground and BP-HiPIMS on PS for effective film thicknesses of 2, 6 and 20 nm. Horizontal red lines in SEM images separate DCMS-ground (top part) and BP-HiPIMS (bottom part). The scalebar applies to all SEM images. (For interpretation of the references to colour in this figure legend, the reader is referred to the web version of this article.)

CRediT authorship contribution statement

Kristian A. Reck: Writing - Original Draft, Conceptualization, Investigation, Formal analysis, Data Curation, Visualization. **Yusuf Bulut:** Writing – review & editing, Investigation. **Zhuijun Xu:** Writing – review & editing, Investigation. **Suzhe Liang:** Writing – review & editing, Investigation. **Thomas Strunskus:** Writing – review & editing, Project administration, Investigation, Conceptualization. **Benedikt Sochor:** Writing – review & editing, Data curation. **Holger Gerdes:** Writing – review & editing, Resources. **Ralf Bandorf:** Writing – review & editing, Resources. **Peter Müller-Buschbaum:** Writing – review & editing, Project administration, Funding acquisition, Conceptualization. **Stephan V. Roth:** Conceptualization, Resources, Writing - Review & Editing, Project administration, Funding acquisition. **Alexander Vahl:** Writing – review & editing, Visualization, Supervision. **Franz Faupel:** Writing – review & editing, Supervision, Resources, Project administration, Funding acquisition, Conceptualization.

Declaration of competing interest

The authors declare that they have no known competing financial interests or personal relationships that could have appeared to influence the work reported in this paper.

Data availability

Data will be made available on request.

Acknowledgments

This work was partially funded by the Deutsche Forschungsgemeinschaft (DFG, German Research Foundation) – project 459798762 (RO 4638/3-1, FA 234/36-1, and MU 1487/39-1). We acknowledge DESY (Hamburg, Germany), a member of the Helmholtz Association HGF, for the provision of beamtime at PETRA III for proposal I-20010005 and I-20211138. S. Liang acknowledges the financial support from the China Scholarship Council (CSC). Z. Xu acknowledges funding from the Deutsche Forschungsgemeinschaft (DFG, German Research Foundation) by the International Research Training Group 2022 Alberta/Technical University of Munich International Graduate School for Environmentally Responsible Functional Hybrid Materials (ATUMS). Special thanks go to Stefan Rehders and Jan Rubeck for technical support.

Appendix A. Supplementary data

Supplementary data to this article can be found online at https://doi.org/10.1016/j.apsusc.2024.160392.

References

[1] L. Polavarapu, K.K. Manga, H.D. Cao, K.P. Loh, Q.-H. Xu, Preparation of conductive silver films at mild temperatures for printable organic electronics, Chem. Mater. 23 (2011) 3273–3276, https://doi.org/10.1021/cm200471s.

[2] L. Kinner, T. Dimopoulos, G. Ligorio, E.J.W. List-Kratochvil, F. Hermerschmidt, High performance organic light-emitting diodes employing ITO-free and flexible TiO x /Ag/Al:ZnO electrodes, RSC Adv. 11 (2021) 17324–17331, https://doi.org/10.1039/D1RA02214H.

[3] M.C. Eze, G. Ugwuanyi, M. Li, H.U. Eze, G.M. Rodriguez, A. Evans, V.G. Rocha, Z. Li, G. Min, Optimum silver contact sputtering parameters for efficient perovskite solar cell fabrication, Sol. Energy Mater. Sol. Cells 230 (2021) 111185, https://doi.org/10.1016/j.solmat.2021.111185.

[4] S.-H. Cho, R. Pandey, C.-H. Wie, Y.J. Lee, J.-W. Lim, D.-H. Park, J.-S. Seok, Y.-H. Jang, K.-K. Kim, D.K. Hwang, D.-J. Byun, W.-K. Choi, Highly transparent ZTO/Ag/ZTO multilayer electrode deposited by inline sputtering process for organic photovoltaic cells, Phys. Status Solidi A 211 (2014) 1860–1867, https://doi.org/10.1002/pssa.201330594.

[5] S.-H. Park, S.-J. Lee, J.H. Lee, J. Kal, J. Hahn, H.-K. Kim, Large area roll-to-roll sputtering of transparent ITO/Ag/ITO cathodes for flexible inverted organic solar cell modules, Org. Electron. 30 (2016) 112–121, https://doi.org/10.1016/j.orgel.2015.12.009.

[6] G. Zhao, W. Shen, E. Jeong, S.-G. Lee, S.M. Yu, T.-S. Bae, G.-H. Lee, S.Z. Han, J. Tang, E.-A. Choi, J. Yun, Ultrathin silver film electrodes with ultralow optical and electrical losses for flexible organic photovoltaics, ACS Appl. Mater. Interfaces 10 (2018) 27510–27520, https://doi.org/10.1021/acsami.8b08578.

[7] Z. Cheng, Y. Wang, D.M. O'Carroll, Influence of partially-oxidized silver back electrodes on the electrical properties and stability of organic semiconductor diodes, Org. Electron. 70 (2019) 179–185, https://doi.org/10.1016/j.orgel.2019.04.015.

[8] D. Ji, L. Jiang, H. Dong, Q. Meng, Y. Zhen, W. Hu, Silver mirror reaction for organic electronics: towards high-performance organic field-effect transistors and circuits, J. Mater. Chem. C 2 (2014) 4142, https://doi.org/10.1039/C4TC00119B.

[9] S.-T. Han, H. Peng, Q. Sun, S. Venkatesh, K.-S. Chung, S.C. Lau, Y. Zhou, V.A. L. Roy, An Overview of the Development of Flexible Sensors, Advanced materials (Deerfield Beach, Fla.) 29 (2017), https://doi.org/10.1002/adma.201700375.

[10] A. Anders, A structure zone diagram including plasma-based deposition and ion etching, Thin Solid Films 518 (2010) 4087–4090, https://doi.org/10.1016/j.tsf.2009.10.145.

[11] T.-T.-N. Nguyen, Y.-H. Chen, Z.-M. Chen, K.-B. Cheng, J.-L. He, Microstructure, near infrared reflectance, and surface temperature of Ti-O coated polyethylene terephthalate fabrics prepared by roll-to-roll high power impulse magnetron sputtering system, Thin Solid Films 663 (2018) 1–8, https://doi.org/10.1016/j.tsf.2018.08.003.

[12] J. Glenneberg, F. Andre, I. Bardenhagen, F. Langer, J. Schwenzel, R. Kun, A concept for direct deposition of thin film batteries on flexible polymer substrate, J. Power Sources 324 (2016) 722–728, https://doi.org/10.1016/j.jpowsour.2016.06.007.

[13] S. Liang, M. Schwartzkopf, S.V. Roth, P. Müller-Buschbaum, State of the art of ultra-thin gold layers: formation fundamentals and applications, Nanoscale Advances 4 (2022) 2533–2560, https://doi.org/10.1039/D2NA00127F.

[14] J. Yun, Ultrathin metal films for transparent electrodes of flexible optoelectronic devices, Adv. Funct. Mater. (2017), https://doi.org/10.1002/adfm.201606641.

[15] V. Tiron, E.-L. Ursu, D. Cristea, D. Munteanu, G. Bulai, A. Ceban, I.-L. Velicu, Overcoming the insulating materials limitation in HiPIMS: Ion-assisted deposition of DLC coatings using bipolar HiPIMS, Appl. Surf. Sci. 494 (2019) 871–879, https://doi.org/10.1016/j.apsusc.2019.07.239.

[16] J.A. Santiago, I. Fernández-Martínez, T. Kozák, J. Capek, A. Wennberg, J. M. Molina-Aldareguia, V. Bellido-González, R. González-Arrabal, M.A. Monclús, The influence of positive pulses on HiPIMS deposition of hard DLC coatings, Surf. Coat. Technol. 358 (2019) 43–49, https://doi.org/10.1016/j.surfcoat.2018.11.001.

[17] D. Lundin, K. Sarakinos, An introduction to thin film processing using high-power impulse magnetron sputtering, J. Mater. Res. 27 (2012) 780–792, https://doi.org/10.1557/jmr.2012.8.

[18] A. Ghailane, M. Makha, H. Larhlimi, J. Alami, Design of hard coatings deposited by HiPIMS and dcMS, Mater. Lett. 280 (2020) 128540, https://doi.org/10.1016/j.matlet.2020.128540.

[19] J. Vetter, T. Shimizu, D. Kurapov, T. Sasaki, J. Mueller, D. Stangier, M. Esselbach, Industrial application potential of high power impulse magnetron sputtering for wear and corrosion protection coatings, J. Appl. Phys. (2023), https://doi.org/10.1063/5.0159292.

[20] J. Keraudy, R.P.B. Viloan, M.A. Raadu, N. Brenning, D. Lundin, U. Helmersson, Bipolar HiPIMS for tailoring ion energies in thin film deposition, Surf. Coat. Technol. 359 (2019) 433–437, https://doi.org/10.1016/j.surfcoat.2018.12.090.

[21] J.T. Gudmundsson, N. Brenning, D. Lundin, U. Helmersson, High power impulse magnetron sputtering discharge, J. Vac. Sci. Technol. A 030801 (2012), https://doi.org/10.1116/1.3691832.

[22] A. Hecimovic, A.P. Ehiasarian, Time evolution of ion energies in HIPIMS of chromium plasma discharge, J. Phys. D: Appl. Phys. 42 (2009) 135209, https://doi.org/10.1088/0022-3727/42/13/135209.

[23] G. Greczynski, J. Lu, M.P. Johansson, J. Jensen, I. Petrov, J.E. Greene, L. Hultman, Role of Tin+ and Aln+ ion irradiation (n=1, 2) during Ti1-xAlxN alloy film growth in a hybrid HIPIMS/magnetron mode, Surf. Coat. Technol. 206 (2012) 4202–4211, https://doi.org/10.1016/j.surfcoat.2012.04.024.

[24] G.T. West, P.J. Kelly, J.W. Bradley, A comparison of thin silver films grown onto zinc oxide via conventional magnetron sputtering and HiPIMS deposition, IEEE Trans. Plasma Sci. 38 (2010) 3057–3061, https://doi.org/10.1109/TPS.2010.2066580.

[25] K. Sarakinos, J. Wördenweber, F. Uslu, P. Schulz, J. Alami, M. Wuttig, The effect of the microstructure and the surface topography on the electrical properties of thin Ag films deposited by high power pulsed magnetron sputtering, Surf. Coat. Technol. 202 (2008) 2323–2327, https://doi.org/10.1016/j.surfcoat.2007.08.028.

[26] R. Bandorf, S. Waschke, F.C. Carreri, M. Vergöhl, G. Grundmeier, G. Bräuer, Direct metallization of PMMA with aluminum films using HIPIMS, Surf. Coat. Technol. 290 (2016) 77–81, https://doi.org/10.1016/j.surfcoat.2015.10.070.

[27] J. Guljakow, W. Lang, Adhesion of HIPIMS-Deposited Gold to a Polyimide Substrate, Coatings 13 (2023) 250, https://doi.org/10.3390/coatings13020250.

[28] Y. Bulut, B. Sochor, C. Harder, K. Reck, J. Drewes, Z. Xu, X. Jiang, A. Meinhardt, A. Jeromin, M. Kohantorabi, H. Noei, T.F. Keller, T. Strunskus, F. Faupel, P. Müller-Buschbaum, S.V. Roth, Diblock copolymer pattern protection by silver cluster reinforcement, Nanoscale 15 (2023) 15768–15774, https://doi.org/10.1039/D3NR03215A.

[29] T. Kozák, A.D. Pajdarová, M. Čada, Z. Hubička, P. Mareš, J. Čapek, Ion energy distributions at substrate in bipolar HiPIMS: effect of positive pulse delay, length and amplitude, Plasma Sources Sci. Technol. 29 (2020) 65003, https://doi.org/10.1088/1361-6595/ab8fbb.

[30] Š. Batková, J. Čapek, J. Rezek, R. Čerstvý, P. Zeman, Effect of positive pulse voltage in bipolar reactive HiPIMS on crystal structure, microstructure and mechanical properties of CrN films, Surf. Coat. Technol. 393 (2020) 125773, https://doi.org/10.1016/j.surfcoat.2020.125773.

[31] R. Ganesan, I. Fernandez-Martinez, B. Akhavan, D. Matthews, D. Sergachev, M. Stueber, D.R. McKenzie, M. Bilek, Pulse length selection in bipolar HiPIMS for high deposition rate of smooth, hard amorphous carbon films, Surf. Coat. Technol. 454 (2023) 129199, https://doi.org/10.1016/j.surfcoat.2022.129199.

[32] F. Avino, D. Fonnesu, T. Koettig, M. Bonura, C. Senatore, A.T. Perez Fontenla, A. Sublet, M. Taborelli, Improved film density for coatings at grazing angle of incidence in high power impulse magnetron sputtering with positive pulse, Thin Solid Films 706 (2020), https://doi.org/10.1016/j.tsf.2020.138058, 138058.

[33] M. Samuelsson, D. Lundin, J. Jensen, M.A. Raadu, J.T. Gudmundsson, U. Helmersson, On the film density using high power impulse magnetron sputtering, Surf. Coat. Technol. 205 (2010) 591–596, https://doi.org/10.1016/j.surfcoat.2010.07.041.

[34] P. Müller-Buschbaum, A basic introduction to grazing incidence small angle X-ray scattering, in: T.A. Ezquerra, M.C. Garcia-Gutierrez, A. Nogales, M. Gomez (Eds.), Applications of Synchrotron Light to Scattering and Diffraction in Materials and Life Sciences, Springer, Berlin, Heidelberg, 2009, pp. 61–90.

[35] J.R. Levine, J.B. Cohen, Y.W. Chung, P. Georgopoulos, Grazing-incidence small-angle X-ray scattering: new tool for studying thin film growth, J. Appl. Crystallogr. 22 (1989) 528–532, https://doi.org/10.1107/S002188988900717X.

[36] M. Schwartzkopf, A. Buffet, V. Körstgens, E. Metwalli, K. Schlage, G. Benecke, J. Perlich, M. Rawolle, A. Rothkirch, B. Heidmann, G. Herzog, P. Müller-Buschbaum, R. Röhlsberger, R. Gehrke, N. Stribeck, S.V. Roth, From atoms to layers: in situ gold cluster growth kinetics during sputter deposition, Nanoscale 5 (2013) 5053–5062, https://doi.org/10.1039/c3nr34216f.

[37] M. Schwartzkopf, G. Santoro, C.J. Brett, A. Rothkirch, O. Polonskyi, A. Hinz, E. Metwalli, Y. Yao, T. Strunskus, F. Faupel, P. Müller-Buschbaum, S.V. Roth, Real-time monitoring of morphology and optical properties during sputter deposition for tailoring metal-polymer interfaces, ACS Appl. Mater. Interfaces 7 (2015) 13547–13556, https://doi.org/10.1021/acsami.5b02901.

[38] S.J. Schaper, F.C. Löhrer, S. Xia, C. Geiger, M. Schwartzkopf, P. Pandit, J. Rubeck, B. Fricke, S. Frenzke, A.M. Hinz, N. Carstens, O. Polonskyi, T. Strunskus, F. Faupel, S.V. Roth, P. Müller-Buschbaum, Revealing the growth of copper on polystyrene-block-poly(ethylene oxide) diblock copolymer thin films with in situ GISAXS, Nanoscale 13 (2021) 10555–10565, https://doi.org/10.1039/d1nr01480c.

[39] M. Schwartzkopf, A. Hinz, O. Polonskyi, T. Strunskus, F.C. Löhrer, V. Körstgens, P. Müller-Buschbaum, F. Faupel, S.V. Roth, Role of sputter deposition rate in tailoring nanogranular gold structures on polymer surfaces, ACS Appl. Mater. Interfaces 9 (2017) 5629–5637, https://doi.org/10.1021/acsami.6b15172.

[40] S. Han, X. Zhuang, W. Shi, X. Yang, L. Li, J. Yu, Poly(3-hexylthiophene)/polystyrene (P3HT/PS) blends based organic field-effect transistor ammonia gas sensor, Sens. Actuators B 225 (2016) 10–15, https://doi.org/10.1016/j.snb.2015.11.005.

[41] G. Amarandei, C. O'Dwyer, A. Arshak, D. Corcoran, The stability of thin polymer films as controlled by changes in uniformly sputtered gold, Soft Matter 9 (2013) 2695, https://doi.org/10.1039/c3sm27130g.

[42] S. Sharma, D. Gahan, P. Scullin, J. Doyle, J. Lennon, R.K. Vijayaraghavan, S. Daniels, M.B. Hopkins, Measurement of deposition rate and ion energy distribution in a pulsed dc magnetron sputtering system using a retarding field analyzer with embedded quartz crystal microbalance, Rev. Sci. Instrum. 87 (2016) 43511, https://doi.org/10.1063/1.4946788.

[43] A. Buffet, A. Rothkirch, R. Döhrmann, V. Körstgens, M.M. Abul Kashem, J. Perlich, G. Herzog, M. Schwartzkopf, R. Gehrke, P. Müller-Buschbaum, S.V. Roth, P03, the microfocus and nanofocus X-ray scattering (MiNaXS) beamline of the PETRA III

storage ring: the microfocus endstation, J. Synchrotron Radiat. 19 (2012) 647–653, https://doi.org/10.1107/S0909049512016895.
[44] G. Benecke, W. Wagermaier, C. Li, M. Schwartzkopf, G. Flucke, R. Hoerth, I. Zizak, M. Burghammer, E. Metwalli, P. Müller-Buschbaum, M. Trebbin, S. Förster, O. Paris, S.V. Roth, P. Fratzl, A customizable software for fast reduction and analysis of large X-ray scattering data sets: applications of the new DPDAK package to small-angle X-ray scattering and grazing-incidence small-angle X-ray scattering, J. Appl. Crystallogr. 47 (2014) 1797–1803, https://doi.org/10.1107/S1600576714019773.
[45] D. Lundin, P. Larsson, E. Wallin, M. Lattemann, N. Brenning, U. Helmersson, Cross-field ion transport during high power impulse magnetron sputtering, Plasma Sources Sci. Technol. 17 (2008) 35021, https://doi.org/10.1088/0963-0252/17/3/035021.
[46] I.-L. Velicu, G.-T. Ianoş, C. Porosnicu, I. Mihăilă, I. Burducea, A. Velea, D. Cristea, D. Munteanu, V. Tiron, Energy-enhanced deposition of copper thin films by bipolar high power impulse magnetron sputtering, Surf. Coat. Technol. 359 (2019) 97–107, https://doi.org/10.1016/j.surfcoat.2018.12.079.
[47] R.P.B. Viloan, J. Gu, R. Boyd, J. Keraudy, L. Li, U. Helmersson, Bipolar high power impulse magnetron sputtering for energetic ion bombardment during TiN thin film growth without the use of a substrate bias, Thin Solid Films 688 (2019) 137350, https://doi.org/10.1016/j.tsf.2019.05.069.
[48] F. Walk, R. Valizadeh, J.W. Bradley, Ion energy analysis of a bipolar HiPIMS discharge using a retarding field energy analyser, Plasma Sources Sci. Technol. 31 (2022) 65002, https://doi.org/10.1088/1361-6595/ac6a0d.
[49] T. Kubart, M. Čada, D. Lundin, Z. Hubička, Investigation of ionized metal flux fraction in HiPIMS discharges with Ti and Ni targets, Surf. Coat. Technol. 238 (2014) 152–157, https://doi.org/10.1016/j.surfcoat.2013.10.064.
[50] D. Lundin, M. Čada, Z. Hubička, Ionization of sputtered Ti, Al, and C coupled with plasma characterization in HiPIMS, Plasma Sources Sci. Technol. 24 (2015) 35018, https://doi.org/10.1088/0963-0252/24/3/035018.
[51] C. Christou, Z.H. Barber, Ionization of sputtered material in a planar magnetron discharge, J. Vac. Sci. Technol. A 18 (2000) 2897–2907, https://doi.org/10.1116/1.1312370.
[52] D.M. Mattox, Handbook of Physical Vapor Deposition (PVD) Processing, second ed., Elsevier Science, Burlington, 2010.
[53] A. Krell, P. Blank, Grain size dependence of hardness in dense submicrometer alumina, J. Am. Ceram. Soc. 78 (1995) 1118–1120, https://doi.org/10.1111/j.1151-2916.1995.tb08452.x.
[54] Q. Ma, L. Li, Y. Xu, J. Gu, L. Wang, Y. Xu, Effect of bias voltage on TiAlSiN nanocomposite coatings deposited by HiPIMS, Appl. Surf. Sci. 392 (2017) 826–833, https://doi.org/10.1016/j.apsusc.2016.09.028.
[55] S. Han, Y. Lee, H. Kim, G. Kim, J. Lee, J.-H. Yoon, G. Kim, Polymer surface modification by plasma source ion implantation, Surf. Coat. Technol. 93 (1997) 261–264, https://doi.org/10.1016/S0257-8972(97)00057-1.